

## Maps of the dynamics of an optically injected solid-state laser

Simo Valling,\* Thomas Fordell, and Åsa Marie Lindberg

*Accelerator Laboratory, Department of Physical Sciences, P.O.Box 64, 00014 University of Helsinki, Helsinki, Finland*

(Received 29 April 2005; published 13 September 2005)

Maps of the dynamics of an optically injected solid-state Nd:YVO<sub>4</sub> laser are presented. Experimental maps showing different dynamical regions are generated automatically from measured intensity time series by plotting the maxima of intensity. Corresponding numerical maps and a bifurcation diagram are calculated with a rate equation model of an injected class B laser. Intensity time series inside different regions in the maps are examined. The experimental and numerical maps are shown to be in good agreement with each other if the linewidth enhancement factor  $\alpha$  is used as a fitting parameter in the model. As a result, experimental estimates for an effective  $\alpha$  are given for a Nd:YVO<sub>4</sub> laser. The effects of noise on the dynamics are also discussed.

DOI: [10.1103/PhysRevA.72.033810](https://doi.org/10.1103/PhysRevA.72.033810)

PACS number(s): 42.65.Sf, 42.55.Xi

### I. INTRODUCTION

In optical injection, light from a master laser is sent to the cavity of the injected slave laser. The controllable parameters in the system are the injection strength  $K$  and the frequency detuning  $\Delta\omega$  between the master laser and the free running injected laser. In class B lasers, external optical injection is known to cause complex dynamics.

An illustrative way to study the dynamics of optically injected lasers is to construct maps showing different dynamical regions in the parameter plane spanned by the injection parameters  $K$  and  $\Delta\omega$ . Detailed experimental maps have been published for Fabry-Pérot type semiconductor lasers [1–3] and for distributed feedback lasers [4,5]. Numerically, maps are calculated either by directly integrating the injected laser rate equations [6–8] or with bifurcation analysis [5,9,10]. In direct integration, some measure of the dynamical state is computed for a large number of points in the  $(K, \Delta\omega)$  plane. In bifurcation analysis, boundaries of different dynamical regions are located and followed.

In the experimental part of this study, the dynamical state of the injected solid state laser is examined with intensity time series. This is different from the case of semiconductor lasers, where experiments rely mostly on optical spectra due to the much shorter time scales. The microsecond time scale of the solid state laser and the use of intensity time series allow continuous measurement of the dynamics while one injection parameter is swept. Time series have been used to investigate injected class B lasers both experimentally with CO<sub>2</sub> [11] and NMR systems [12] and numerically (see, e.g., [13,14]).

In this paper, maps of the dynamics of an optically injected solid state Nd:YVO<sub>4</sub> laser are presented. A method based on maximum amplitudes of the intensity time series is used to distinguish different dynamical regions in the  $(K, \Delta\omega)$  plane. The same method is also utilized numerically with a rate equation model of an injected class B laser. Finally, the model is studied with bifurcation analysis.

Experimental mappings of the solid state laser dynamics have not been reported so far. Experimental studies on in-

jected solid state lasers have concerned mainly injection locking, including works on noise properties (e.g., [15,16]) and chaos synchronization [17,18]. Theoretically, solid state laser dynamics in injection has been studied recently [9,19–21].

The dynamics of an injected class B laser is greatly affected by the linewidth enhancement factor  $\alpha$ . In semiconductor lasers  $\alpha$  is typically between 2 and 7, whereas it is expected to be near zero in solid state and CO<sub>2</sub> lasers. In solid state lasers, precise experimental values for the  $\alpha$  factor have not been published, although, evidence has been given recently that  $\alpha$  can take a rather large value ( $\approx 1$ ) in a microchip laser [22]. To get an agreement between experimental and numerical maps in this paper, experimental estimates are found for an effective  $\alpha$  factor in a Nd:YVO<sub>4</sub> laser. As a result, mapping the dynamics constitutes a way of experimentally determining the value of  $\alpha$ . Also shown is that the effective  $\alpha$  may change. The explicit origin of  $\alpha$  in solid state lasers will be an interesting topic for future studies.

This paper is organized as follows: in the next section the experimental setup is presented together with the method used to acquire intensity time series of the injected laser. The model and the measurement of its parameters are introduced in Sec. III. The experimental maps are compared to the simulated maps and to the bifurcation diagram in Sec. IV. Experimental intensity time series in a few specific dynamical regions are plotted with their numerical counterparts in Sec. V. Conclusions are given in Sec. VI.

### II. EXPERIMENTAL SETUP

Figure 1 shows the experimental setup for optical injection. Two solid state lasers are operated in a master-slave configuration. Both lasers are 1 mm thick Nd:YVO<sub>4</sub> crystals (CASIX) pumped with 150 mW SDL diode lasers at 809 nm. Feedback to the pump laser diodes is blocked with Faraday isolators. The crystals are mounted to copper mounts to allow temperature control. Remaining pump light after the crystals is removed from the 1064 nm beams with interference filters. The Faraday isolators make the coupling between the master and slave lasers unidirectional and prevent unwanted feedback. The injection beam from the master la-

\*Electronic address: [simo.valling@helsinki.fi](mailto:simo.valling@helsinki.fi)

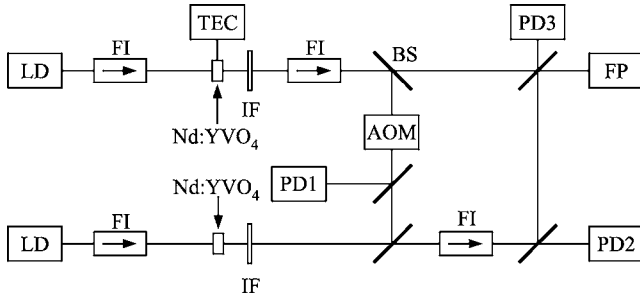


FIG. 1. Experimental setup: LD, laser diode; FI, Faraday isolator; TEC, temperature control; IF, interference filter; BS, beam splitter; AOM, acousto-optic modulator; FP, Fabry-Pérot interferometer; PD's, photodetectors.

ser is directed into the cavity of the slave laser through an acousto-optic modulator (AOM) and the injection power is measured after the AOM with the detector PD1.

Optical spectra are recorded with a 150 GHz free spectral range scanning Fabry-Pérot interferometer (Burleigh TL-15) to ensure single mode operation of both lasers and to enable coarse frequency tuning. The beat frequency between the lasers is measured with a home-made 400 MHz photodetector PD3 and the optical input (PD2) of a Tektronix CSA 7404 oscilloscope is used to measure intensity time series of the injected laser.

The relaxation oscillation frequency and output power of the master laser are 4 MHz and 8 mW, respectively. An optoelectronic feedback loop (not shown in Fig. 1) is employed to suppress the relaxation oscillation peak of the master laser intensity noise spectrum [23]. The temperature of the master laser is tuned with a Peltier element to control the frequency detuning between the lasers. The slave laser is pumped 3.5 times above threshold, resulting in an output power of 8 mW and a relaxation oscillation frequency of 3.5 MHz.

The measurement of the intensity time series of the injected slave laser is realized in the following way. For a fixed frequency detuning, the injection power is modulated using an AOM. The slave laser intensity time series (PD2), the time series of the beat frequency (PD3) and the measured injection power (PD1) are all coupled to the three channels of the same oscilloscope. As a result, the intensity time series of the injected laser are recorded as a function of the injection power and the beat frequency is picked up for each time series.

The injection strength that is needed to achieve locking in solid state lasers increases linearly with the frequency detuning (the locking region is the white area in Figs. 4 and 5). Moreover, once the locking range is entered, further increase in injection power does not change the state of the injected laser. Consequently, if an injection power sweep starts from zero and continues until locking is reached, all the waveforms of the dynamics for the corresponding frequency detuning are captured in a single intensity trace. Figure 2 presents an example of an intensity time trace recorded in such a way. The use of triangle wave modulation enables direct observation of possible hysteresis in the dynamics by comparing the results with increasing and decreasing injection power. These time traces captured for a large number of dif-

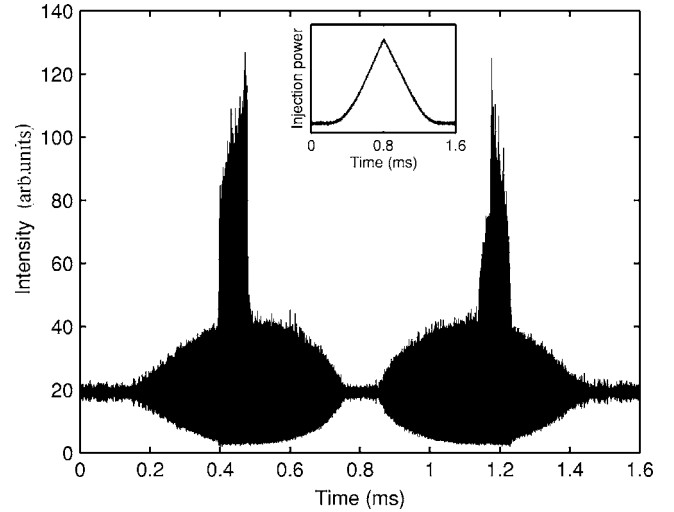


FIG. 2. An example of an intensity time trace during a single injection power sweep. The frequency detuning is approximately 1.4 times the relaxation oscillation frequency of the injected laser. The injection power is zero at  $t=0$  ms and at  $t=1.6$  ms and it is increasing when  $t < 0.8$  ms and decreasing after  $t > 0.8$  ms as shown in the inset. The intensity time trace around 0.8 ms corresponds to locking.

ferent frequency detunings contain all the data needed to construct the experimental maps presented in Sec. IV.

### III. THE MODEL

The experimental results are compared to a phenomenological single mode rate equation model of a class B laser [7,24]

$$\begin{aligned} \frac{da}{dt} &= \left[ \frac{1}{2}(1 - i\alpha) \frac{\gamma_c \gamma_n}{\gamma_s \tilde{J}} (n - 1) - \frac{1}{2} \gamma_p (a^2 - 1) + i\Omega \right] a + \kappa + F_a \\ \frac{dn}{dt} &= \gamma_s (1 - n) + \gamma_s \tilde{J} (1 - a^2) + \gamma_n a^2 (1 - n) + \frac{\gamma_p \gamma_s \tilde{J}}{\gamma_c} a^2 (a^2 - 1) \\ &\quad + F_n, \end{aligned} \quad (1)$$

where  $a$  and  $n$  are the amplitudes of the slowly varying field envelope and the population inversion density, both normalized to their steady state values,  $\tilde{J} = (J - J_{th})/J_{th}$  is the pump power  $J$  normalized to the threshold value  $J_{th}$ ,  $\alpha$  is the linewidth enhancement factor,  $\gamma_c$  and  $\gamma_s$  are the decay rates for the cavity and for the upper laser level,  $\gamma_n$  and  $\gamma_p$  are the relaxation rates for the differential and nonlinear gain. The experimentally controllable injection parameters  $\kappa$  and  $\Omega = 2\pi(\nu_{ML} - \nu_{SL})$  stand for the coupling of the injected field and the angular frequency detuning between the master and the slave lasers, respectively. Noise is introduced into the system through the Gaussian white noise source terms  $F_a$  and  $F_n$ .

The parameter values for the model have been estimated with the following procedure. The 90  $\mu$ s lifetime of the upper laser level [25] gives  $\gamma_s = 1.11 \times 10^4$  s $^{-1}$ . An approxima-

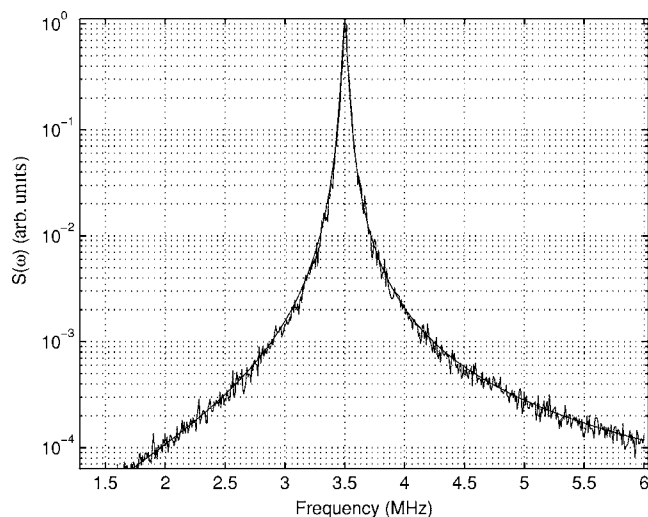


FIG. 3. Experimental power spectrum and the calculated spectrum from Eq. (2). Approximation  $D_n^2 \approx 0$  is used due to the shape of the experimental spectrum.  $S(\omega)$  is normalized with the peak value at 3.5 MHz.

tion for  $\gamma_n$  is given by the relation  $\gamma_n \approx \gamma_s \tilde{J}$ . The cavity decay rate is then obtained from  $\gamma_c \approx \Omega_R^2 / \gamma_n$ , where  $\Omega_R = 2\pi f_R$  is the angular relaxation oscillation frequency. Once  $\gamma_n$  and  $\gamma_s$  are known, the nonlinear gain relaxation rate  $\gamma_p$  is found from the power spectral density

$$S(\omega) = \frac{\left(\frac{\gamma_c \gamma_n}{\gamma_s \tilde{J}}\right)^2 D_n^2 + 4D_a^2(\omega^2 + (\gamma_s + \gamma_n)^2)}{(\Omega_R^2 - \omega^2)^2 + \omega^2 \gamma_r^2}, \quad (2)$$

where

$$\gamma_r = \gamma_s + \gamma_n + \gamma_p, \quad D_n^2 = \langle F_n(\omega) F_n(\omega)^* \rangle, \quad D_a^2 = \langle F_a(\omega) F_a(\omega)^* \rangle$$

and where  $\langle \cdot \rangle$  indicates a time average. A value for  $\gamma_p$  is obtained by fitting the calculated power spectral density to the measured one. Both the measured and the fitted power spectra are presented in Fig. 3. Based on the shape of the measured power spectrum,  $F_a$  is the dominant noise source, see, e.g., [26] for details. Finally,  $D_a$  is calculated from the variance of the output power  $\langle \Delta p^2 \rangle$ . Neglecting the minor noise term  $D_n^2$ ,

$$\langle \Delta p^2 \rangle = \frac{1}{2\pi} \int_{-\infty}^{\infty} S(\omega) d\omega \approx \frac{4D_a^2}{2\pi} \int_{-\infty}^{\infty} \frac{\omega^2 + (\gamma_s + \gamma_n)^2}{(\Omega_R^2 - \omega^2)^2 + \omega^2 \gamma_r^2} d\omega. \quad (3)$$

The parameter values obtained above are summarized in Table I. The linewidth enhancement factor  $\alpha$  is the only undetermined parameter. The  $\alpha$  factor, which couples gain variations to the refractive index, arises from an asymmetric gain profile or from a detuning of the lasing mode from the gain line center. In solid state lasers  $\alpha < 1$  is expected and used in simulations [9,19,27], although, no precise measured values have been published. Based on the symmetric form of the locking region shown in the next section,  $\alpha < 0.6$ . On the other hand,  $\alpha > 0$  is required due to the experimentally observed asymmetry in the dynamics above and below the locking region [9,10]. In order to reach a good agreement between the experiments and the model,  $\alpha$  between 0.2 and 0.35 must be chosen in the simulations of this paper.

The above rate equations contain complex dynamics and multistability. Multistable regions complicate the comparison between experimental and numerical results since the found attractors may depend on the chosen initial conditions. To minimize such problems, the used integration scheme mimics the experimental procedure. To be more precise, the injection strength  $\kappa$  is increased from zero while keeping the angular frequency detuning  $\Omega$  constant. When  $\kappa$  is increased, the initial condition is taken as the last point found for the previous  $\kappa$ .

In addition to the direct integration of the rate equations, the model is also investigated with bifurcation analysis, a powerful tool in the study of dynamical systems. In direct integration, a measure of the dynamical state, e.g., Lyapunov exponent, is calculated in a large number of points in the injection parameter plane to find different dynamical regions. Therefore, good resolution means time-consuming simulations. In bifurcation analysis, a different method is used; boundaries of dynamical regions are detected and then followed. The resulting bifurcation diagram gives a global view on laser dynamics. A detailed review of bifurcation analysis of laser dynamics can be found in [28,29]. In this paper, the Matlab package Matcont [30] is used to construct the bifurcation diagram.

In the next sections, results are given in terms of the normalized injection strength  $K = \kappa / \Omega_R$  and the normalized frequency detuning  $\Delta\omega = \Omega / \Omega_R$ . These commonly used dimensionless injection parameters make the comparison of the results to other reports easier.

TABLE I. Parameter values used in the simulations.

Parameter	Symbol	Value
Relaxation oscillation frequency	$f_R$	3.5 MHz
Normalized pump power	$\tilde{J}$	2.5
Cavity decay rate	$\gamma_c$	$1.7 \times 10^{10} \text{ s}^{-1}$
Atomic decay rate	$\gamma_s$	$1.11 \times 10^4 \text{ s}^{-1}$
Differential gain relaxation rate	$\gamma_n$	$2.78 \times 10^4 \text{ s}^{-1}$
Nonlinear gain relaxation rate	$\gamma_p$	$3.0 \times 10^5 \text{ s}^{-1}$
Langevin noise spectral density	$D_a^2$	$750 \text{ s}^{-1}$

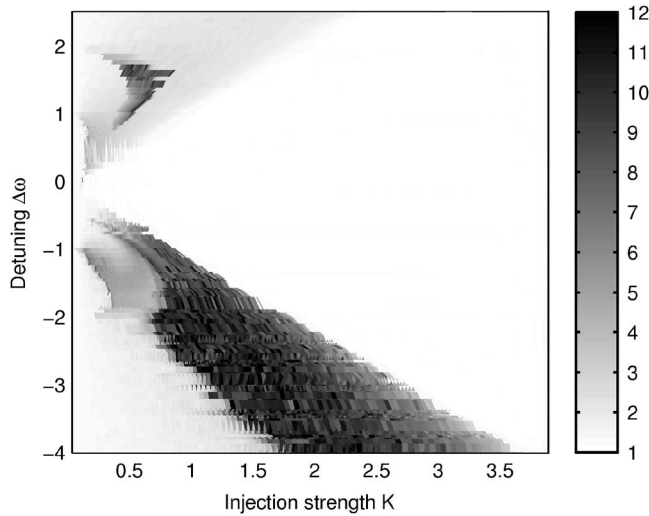


FIG. 4. Experimental map, where the color coding reveals the intensity time series maximum for certain  $(K, \Delta\omega)$ .

#### IV. MAPS

In this section, maps showing different dynamical regions are presented for an injected Nd:YVO<sub>4</sub> laser. Experimental maps based on intensity time series maxima are compared with the corresponding numerical maps. The maps are also compared with the bifurcation diagram.

An experimental map of intensity time series maxima is presented in Fig. 4. The map is constructed as follows. Traces like the one presented in Fig. 2 are first recorded for a large number of different detunings. Each trace contains all intensity waveforms for a specific frequency detuning when the injection strength is increased from zero until locking is observed. The traces are then divided into subintervals corresponding to different values of the injection strength  $K$ . For each subinterval, which consists of several periods of oscillating intensity, the largest maximum of the intensity time series is recorded. The intensity time series maxima found in such a way are then plotted as a function of the injection strength, side by side for a large number of frequency detunings to generate the map shown in Fig. 4. As a result, Fig. 4 represents the maxima of intensity time series in the  $(K, \Delta\omega)$  plane. The maxima are normalized with the free running laser intensity ( $=1$ ). The white color ( $=1$ ) in the maps means that the laser has the same intensity as in the free running case. The black ( $=12$ ) end of the color scale means that the maximum peak heights of the intensity time series are about twelve times the free running value. All the intensity maxima maps presented in this paper are color coded similarly to allow comparisons between them.

Numerical maps representing intensity time series maxima are constructed likewise. Intensity time series are integrated at numerous points in the  $(K, \Delta\omega)$  plane and the maximum value of each time series is recorded. Numerical map of intensity time series maxima for  $\alpha=0.35$  is presented in Fig. 5.

Because the absolute value of the injection strength could not be measured reliably, the experimentally obtained relative injection strength, i.e., the square root of relative injec-

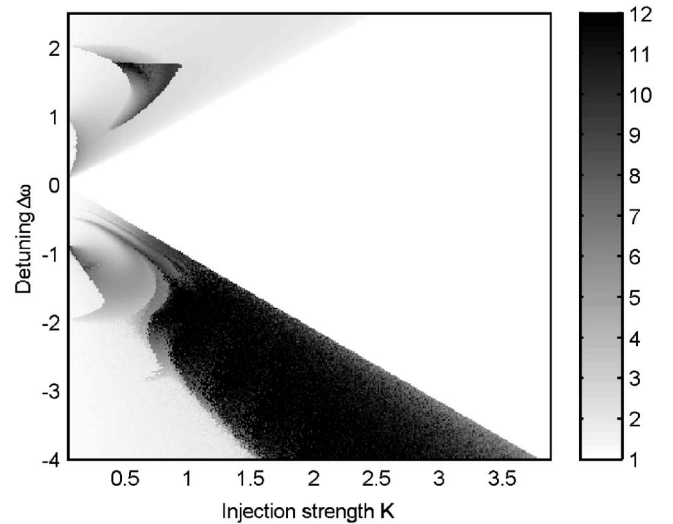


FIG. 5. Numerical map of intensity time series maxima with  $\alpha=0.35$ .

tion power, was normalized to  $K$  in the model by matching the lower locking range boundary to the corresponding boundary in the simulations. With a value of 0.35 for the fitted effective  $\alpha$  in simulations, an agreement between the experimental and the numerical map is observed in the shapes of different regions. The maximum intensities are also similar, slight differences are observed in the dark regions corresponding to high intensity maxima. To be more precise, the intensities given by the model are somewhat higher than the measured ones.

The triangular white region in the middle of the maps of Figs. 4 and 5 corresponds to locking. The injection strength needed to reach the locking range is observed to increase linearly with the frequency detuning. The intensity in the locked state is approximately the same as the free running laser intensity. In the large dark region below the lower locking range boundary, pulsed intensity with peak heights above ten times the free running value are observed. Light or gray regions on the maps typically correspond to periodic sinusoidal oscillations. Inside the dark, crescent-shaped region above the upper locking range boundary, oscillations are born with twice the basic period.

As it is demonstrated in Figs. 4 and 5, the intensity time series maxima of an injected solid state laser are successfully described with the rate equation model used. Next it is shown that mapping the maxima of intensity time series is a suitable method for distinguishing different dynamical regions in the  $(K, \Delta\omega)$  plane. For that purpose, bifurcation analysis is employed with the same model without the noise term. In Fig. 6, a bifurcation diagram with principal bifurcations for  $\alpha=0.35$  is shown. Hopf (H), saddle-node (SN), period-doubling (PD), and torus (T) bifurcations are identified, supercritical bifurcations are plotted with solid lines and subcritical ones with dashed lines. For torus bifurcation curves plotted with gray lines, the stability is unclear due to very small normal form coefficients found with Matcont. Comparison between the bifurcation diagram and the maximum intensity maps reveals that all the numerically obtained bifurcation curves shown in Fig. 6 have their counterparts in

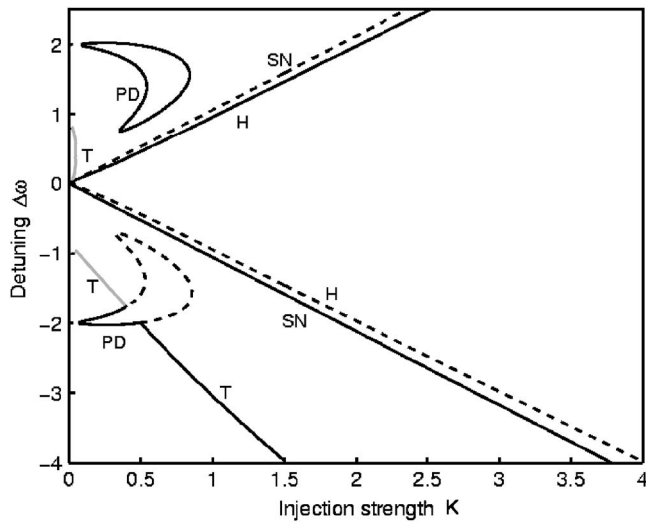


FIG. 6. Bifurcation diagram with  $\alpha=0.35$ . H, Hopf; SN, saddle-node; T, torus; PD, period-doubling. Supercritical bifurcations are plotted with solid black lines and subcritical bifurcations with dashed lines. Gray lines stand for unclear stability of a bifurcation.

the boundaries of different regions in the experimental map in Fig. 4.

The role of  $\alpha$  in the dynamics of an injected class B laser can be emphasized by comparing the bifurcation diagram of Fig. 6 to those calculated for different  $\alpha$  values and for typical semiconductor laser parameters in [9,10]. Despite the totally different laser parameters, it is the  $\alpha$  that makes the bifurcation diagrams similar. For this reason, special attention must be paid to the experimental determination of  $\alpha$  for the model of an injected laser.

In Fig. 7, an experimental map is presented for another measurement where the operating point of the injected laser, determined by the output power and  $\Omega_R$ , is the same as that in the preceding experiment. The map is, however, slightly different compared to Fig. 4. There is one extra detail at about  $(K, \Delta\omega)=(0.3, -1)$ . This detail and the slight shift of the torus curve to the right can be achieved with a smaller  $\alpha$

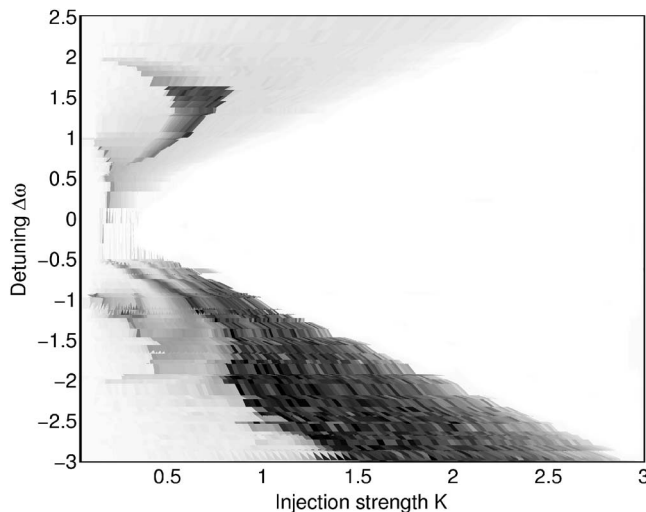


FIG. 7. Experimental map of time series maxima.

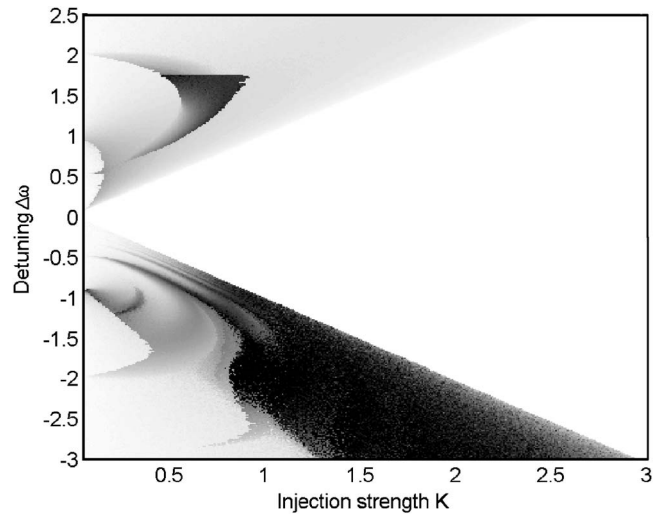


FIG. 8. Numerical map of time series maxima with  $\alpha=0.2$ .

in the simulations. In Fig. 8,  $\alpha=0.2$  is used. Again, agreement between the measurements and the simulations is observed. Thus, it is demonstrated that the  $\alpha$  needed to correctly model the injected Nd:YVO<sub>4</sub> laser may change between measurements. This may be due to changes in parameters like lasing frequency, temperature or exact pumping conditions. The aim here is to point out that the effective  $\alpha$  factor cannot be assumed to be constant for a Nd:YVO<sub>4</sub> laser.

To illustrate the resolution of the experimental maps obtainable with the intensity maxima method used, a map based on another measurement with better resolution is presented in Fig. 9. The experimental parameters used are the same as in the map of Fig. 7 and the map shown can therefore be thought of as a zoom of Fig. 7. Enhanced resolution comes from the larger number of different detunings measured compared to maps in Figs. 4 and 7. The resolution in the detuning axis is limited by the number of measurements and ultimately by the  $\pm 100$  kHz accuracy of the measured frequency detuning. The injection strength is measured con-

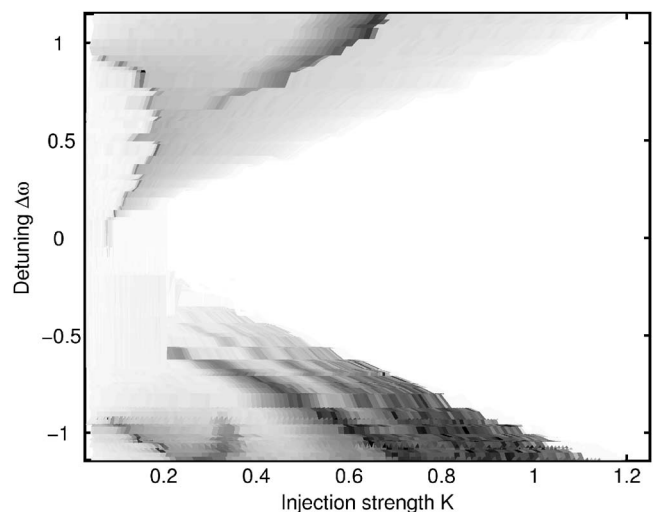


FIG. 9. A detailed experimental map of time series maxima.

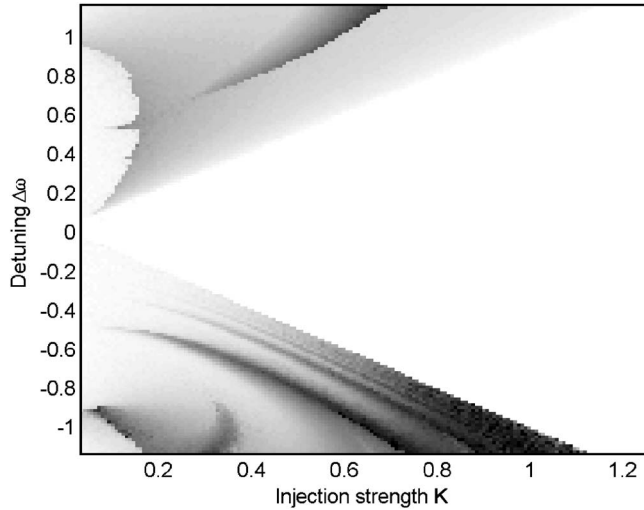


FIG. 10. A detailed numerical map of time series maxima with  $\alpha=0.2$ .

tinuously, the accuracy is limited by the uncertainties in the measurements of the relative injection power and the normalization of the power to  $K$ . As a result, the resolution and accuracy of the intensity maxima map presented in Fig. 9 is better than 0.05 in terms of  $K$  and  $\Delta\omega$ . Comparable resolution can be achieved in any range of parameters  $(K, \Delta\omega)$ , i.e., for larger maps as well. In Fig. 10, the corresponding numerical map is shown with  $\alpha=0.2$ . All the details of the numerical map can be found clearly in the experimental map and vice versa.

## V. INTENSITY TIME SERIES

It has been shown in the preceding section that the shapes of different dynamical regions in  $(K, \Delta\omega)$  plane as well as

the intensity time series maxima for certain injection parameters coincide well with each other in the experiments and in the simulations. Moreover, the boundaries of different regions in the intensity maxima maps in Figs. 4 and 5 have their counterparts in the bifurcation diagram of Fig. 6. The distinction between bifurcation analysis and the intensity maxima method is that the latter only distinguishes the different regions. In order to experimentally specify the corresponding dynamical states, intensity time series must be examined more closely inside each region. In Fig. 11, experimental (above) and numerical (below) intensity time series are compared in different regions of the maps for  $\alpha=0.35$ . The injection parameter values  $(K, \Delta\omega)$  used in the simulations are given for each time series in 11(a2) to 11(f2). The corresponding experimental values in 11(a1) to 11(f1) differ at most 0.05 from the numerical ones.

Figures 11(a1) and 11(a2) present relaxation oscillations of a free running laser in the absence of the injected field. The amplitude of the oscillations gives an insight into the noise level of the laser because relaxation oscillations build up from noise. Typical time series corresponding to a limit cycle are presented in Figs. 11(b1) and 11(b2). In the maps this dynamical region covers almost the whole area above the supercritical Hopf bifurcation for positive detunings and below the torus bifurcation for negative detunings. A periodic sinusoidal signal is observed, the parameters used in this specific case are  $(K, \Delta\omega)=(1.5, 2.3)$ . In Figs. 11(c1) and 11(c2), the time series of a torus are shown with the injection parameters  $(K, \Delta\omega)=(1.32, -3.6)$ . The waveforms shown are typical along the stable torus bifurcation curve shown in Fig. 6. Between the torus bifurcation and the supercritical saddle-node bifurcation that corresponds to the lower locking range boundary, a vast dark region is seen in Figs. 4 and 5 that suggests high intensity time series maxima. Indeed, large pulsed oscillations are observed, examples of which are shown in Figs. 11(d1) and 11(d2). Intensity time series inside

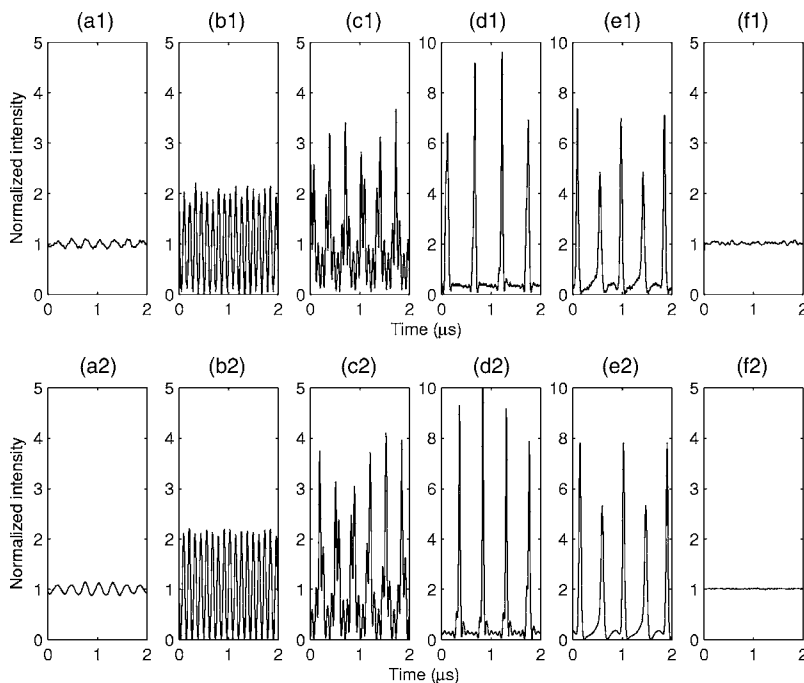


FIG. 11. Experimental (above) and numerical (below) intensity time series in different dynamical regions. Injection parameters  $(K, \Delta\omega)$  from (a2) to (f2) are  $(0, -3.6)$ ,  $(1.5, 2.3)$ ,  $(1.32, -3.6)$ ,  $(1.8, -3.6)$ ,  $(0.6, 1.55)$ , and  $(3.7, -3.6)$ , respectively.

the stable period-doubling bifurcation curve with positive detunings are plotted in Figs. 11(e1) and 11(e2) with  $(K, \Delta\omega) = (0.6, 1.55)$ . Finally in Figs. 11(f1) and 11(f2), typical time series are plotted that correspond to locking. In the bifurcation diagram, the locking region is the area between the supercritical parts of Hopf and saddle-node bifurcations.

As is shown in Fig. 11, not only the dynamical regions of the model and experiments are equal but also the time series. Both the amplitude and the oscillation frequency of the numerical and the experimental time series are in good agreement with each other. Small differences are obtained due to the random nature of noise both in experiments and simulations. In addition, in the time series in Fig. 11 that correspond to locking, the experimental time series 11(f1) has some extra noise compared to the simulations in 11(f2). This is due to the fact that in the simulations the master laser power is stable. In experiments, however, the master laser exhibits some relaxation oscillations even though an electronic feedback loop is used to suppress them.

The  $\alpha$  factor and the noise term are of major importance in the model in order to get a good agreement with the experiments. The  $\alpha$  factor is mainly responsible for the shapes and sizes of the dynamical regions in the maps. In the states with large amplitude oscillations, that is between the stable torus bifurcation curve and the lower locking range boundary, the peak heights and intervals are greatly reduced by the noise term.

Intensity time series of an injected Nd:YVO<sub>4</sub> laser are also reported in [31]. Routes to locking when the injection strength is increased are presented there for different frequency detunings.

## VI. CONCLUSIONS

Maps of the dynamics of an optically injected Nd:YVO<sub>4</sub> laser are presented. Experimentally constructed maps where intensity time series maxima are plotted in the  $(K, \Delta\omega)$  plane are shown to be in agreement with the rate equation model used in the simulations. In addition, the found boundaries of dynamical regions are demonstrated to correspond to the bifurcation curves obtained with bifurcation analysis of the same model. The intensity time series maxima method is thus shown to be a convenient experimental way to map the dynamical states of an injected solid state laser. Compared to the maps based on optical spectra used typically with semiconductor lasers, the following advantage is achieved: the intensity maxima maps are constructed directly from the raw

data without human-made decisions on where the boundaries of the dynamical regions are. This allows a large amount of data to be analyzed straightforwardly, leading to a good resolution. The resolution of the method presented in this paper is better than 0.05 in terms of the normalized injection parameters  $K$  and  $\Delta\omega$ . On the other hand, the intensity maxima do not directly reveal the dynamical states of distinct regions on the maps. To accomplish that, intensity time series must be examined more closely inside each region. In this paper, a good correspondence is demonstrated between experimental and numerical time series both in waveforms and in amplitudes.

To reach an agreement with the experiments, estimates are found for the linewidth enhancement factor  $\alpha$  in the model. Matching the maps leads to an error of at most 0.10 for  $\alpha$ . It is also shown that  $\alpha$  for a Nd:YVO<sub>4</sub> laser may vary between measurements even if the same operating point, determined by the output power and  $\Omega_R$ , is used. It has to be pointed out here that the values presented should be considered as an effective  $\alpha$ ; the origin of  $\alpha$  in solid state lasers may be different to that in semiconductor lasers, and it will be an interesting topic for future studies.

The noise term must be included into the model to properly describe the laser studied in this paper. In the model, the noise is only added to the injected slave laser and the master laser noise contribution is neglected. It can be assumed that the effects of the master laser noise on the maps are smaller but somewhat similar to those observed with the slave laser; the peak heights decrease in pulsed regions. The small contribution of master laser noise could be responsible for the slight difference between experimental and numerical peak heights. Generally, due to noise some of the interesting dynamics may be blurred by random effects.

In this paper, maxima of the intensity time series are mapped to distinguish different dynamical regions, meaning that only a fraction of the data recorded is actually used in the analysis. By computing suitable quantities that change at the bifurcation boundaries, the method introduced offers the possibility to automatically construct a detailed experimental bifurcation diagram of the injected laser.

## ACKNOWLEDGMENTS

Financial support from the Academy of Finland Project No. 77582, the Finnish Academy of Science and Letters, Vilho, Yrjö and Kalle Väisälä Foundation, Magnus Ehrnrooth Foundation, Svenska Kulturfonden and Finska Vetenskaps-societen is acknowledged.

- 
- [1] T. B. Simpson, J. M. Liu, K. F. Huang, and K. Tai, *Quantum Semiclass. Opt.* **9**, 765 (1997).
  - [2] S. Eriksson and Å. M. Lindberg, *J. Opt. B: Quantum Semiclassical Opt.* **4**, 149 (2002).
  - [3] S. Eriksson, *Opt. Commun.* **210**, 343 (2002).
  - [4] T. B. Simpson, *Opt. Commun.* **215**, 135 (2003).
  - [5] S. Wieczorek, T. B. Simpson, B. Krauskopf, and D. Lenstra,

*Phys. Rev. E* **65**, 045207(R) (2002).

- [6] K. E. Chlouverakis and M. J. Adams, *Opt. Commun.* **216**, 405 (2003).
- [7] T. Fordell and Å. M. Lindberg, *Opt. Commun.* **242**, 613 (2004).
- [8] S. K. Hwang and J. M. Liu, *Opt. Commun.* **183**, 195 (2000).
- [9] B. Krauskopf and S. Wieczorek, *Physica D* **173**, 97 (2002).

- [10] S. Wieczorek, B. Krauskopf, and D. Lenstra, *Opt. Commun.* **172**, 279 (1999).
- [11] J. L. Boulnois, A. van Lerberghe, P. Cottin, F. T. Arecchi, and G. P. Puccioni, *Opt. Commun.* **58**, 124 (1986).
- [12] E. Brun, B. Derighetti, D. Meier, R. Holzner, and M. Ravani, *J. Opt. Soc. Am. B* **2**, 156 (1985).
- [13] J. R. Tredicce, F. T. Arecchi, G. L. Lippi, and G. P. Puccioni, *J. Opt. Soc. Am. B* **2**, 173 (1985).
- [14] L. A. Lugiato, L. M. Narducci, D. K. Bandy, and C. A. Pennise, *Opt. Commun.* **46**, 64 (1983).
- [15] A. Bramati, J.-P. Hermier, V. Jost, and E. Giacobino, *Eur. Phys. J. D* **19**, 421 (2002).
- [16] C. C. Harb, T. C. Ralph, E. H. Huntington, I. Freitag, D. E. McClelland, and Hans-A. Bachor, *Phys. Rev. A* **54**, 4370 (1996).
- [17] A. Uchida, T. Ogawa, and F. Kannari, *Rev. Laser Eng.* **26**, 881 (1998).
- [18] A. Uchida, S. Kinugawa, T. Matsuura, and S. Yoshimori, *Phys. Rev. E* **67**, 026220 (2003).
- [19] E. G. Lariontsev, I. Zolotoverkh, P. Besnard, and G. M. Stéphan, *Eur. Phys. J. D* **5**, 107 (1999).
- [20] M. K. Stephen Yeung and S. H. Strogatz, *Phys. Rev. E* **58**, 4421 (1998); M. K. Stephen Yeung and S. H. Strogatz, *Phys. Rev. E* **61**, 2154(E)(2000).
- [21] M. G. Zimmermann, M. A. Natiello, and H. G. Solari, *Chaos* **11**, 500 (2001).
- [22] C. Szwaj, E. Lacot, and O. Hugon, *Phys. Rev. A* **70**, 033809 (2004).
- [23] S. Valling, B. Ståhlberg, and Å. M. Lindberg, *Opt. Laser Technol.* (to be published).
- [24] T. B. Simpson, J. M. Liu, A. Gavrielides, V. Kovanis, and P. M. Alsing, *Appl. Phys. Lett.* **64**, 3539 (1994).
- [25] CASIX Crystal Guide (1999).
- [26] C. Becher and K.-J. Boller, *J. Opt. Soc. Am. B* **16**, 286 (1999).
- [27] T.-S. Lim, T.-H. Yang, J.-L. Chern, and K. Otsuka, *IEEE J. Quantum Electron.* **37**, 1215 (2001).
- [28] *Fundamental Issues of Nonlinear Laser Dynamics: Concepts, Mathematics, Physics and Applications*, edited by B. Krauskopf and D. Lenstra, AIP Conf. Proc. No. 548 (AIP, Melville, 2000).
- [29] S. Wieczorek, Ph.D. thesis, Vrije Universiteit Amsterdam, 2002.
- [30] A. Dhooge, W. Govaerts, and Yu. A. Kuznetsov, *ACM Trans. Math. Softw.* **29**, 141 (2003).
- [31] S. Valling, T. Fordell, and Å. M. Lindberg, *Opt. Commun.* (to be published).